J. Appl. Comput. Mech., 7(3) (2021) 1737-1750
DOI: 10.22055/JACM.2021.37406.3011

ISSN: 2383-4536
jacm.scu.ac.ir

Shahid Chamran University of Ahvaz

Journal of Applied and Computational Mechanics

Research Paper

An Experimental and Numerical Study on the Aerodynamic Performance of Vibrating Wind Turbine Blade with Frequency-Domain Method

Shine Win Naung[1], Mahdi Erfanian Nakhchi[2], Mohammad Rahmati[3]

[1] Department of Mechanical and Construction Engineering, Northumbria University, Newcastle, Upon Tyne, NE1 8ST, United Kingdom, Email: shine.naung@northumbria.ac.uk

[2] Department of Mechanical and Construction Engineering, Northumbria University, Newcastle, Upon Tyne NE1 8ST, United Kingdom, Email: mahdi.nakhchi@northumbria.ac.uk

[3] Department of Mechanical and Construction Engineering, Northumbria University, Newcastle Upon Tyne NE1 8ST, United Kingdom, Email: mohammad.rahmati@northumbria.ac.uk

Received May 11 2021; Revised June 01 2021; Accepted for publication June 03 2021.
Corresponding author: M. Rahmati (mohammad.rahmati@northumbria.ac.uk)

Abstract. A highly efficient nonlinear frequency-domain solution method is proposed and employed to investigate the aerodynamic and aeromechanical performances of an oscillating wind turbine blade aerofoil in this study. Extensive validations of a frequency-domain method against an experiment as well as a typical time-domain solution method are provided in this paper. An experiment is also designed and conducted to measure pressure distributions over an aerofoil as well as to validate the numerical model. Unsteady pressure distributions and aeroelasticity parameters of the oscillating NACA0012 aerofoil are computed at various angles of attack and Reynolds numbers. Results indicate that the difference of unsteady pressure distributions between the two surfaces of the aerofoil becomes larger as the angle of attack is increased, whereas the flow separation on the suction surface is reduced by raising the Reynolds number. The turbulent flow develops in the downstream region due to the laminar vortex shedding at lower Reynolds numbers. It is also revealed that the Reynolds number has an impact on the aeroelasticity, and the aerodynamic damping value is larger at higher Reynolds numbers. The comparison between the frequency-domain method and the time-domain method shows that the frequency-domain method is not only accurate but also computationally very efficient as the computation time is reduced by 90%.

Keywords: Wind turbine; Vibrations; NACA-0012; Aerodynamic damping; Frequency-domain method.

1. Introduction

The interaction between the aerodynamic load and the elastic blade structure is the main reason for aeroelastic instability problems in wind turbines (WT) [1]. In the past decade, the lengths of wind turbine blades were expanded to obtain wind energy more effectively. Due to the design of extremely long and flexible blades with less weight, modern wind turbine blades possess lower structural damping values, which leads to instabilities in the structure when excited by the external aerodynamic loads [2]. Hence, the structural stability of the blade has been the focus of many research studies aiming to enhance structural damping [3]. Apart from the structural damping, aerodynamic damping is also required for the design of the blades. Aerodynamic damping determines whether the blade vibration, excited by aerodynamic forces, is damped [4]. Therefore, the aeroelasticity model coupling the structural and aerodynamic calculations is required to ensure the mechanical integrity of wind turbines [4].

Potential aeroelastic instability problems that can happen in advanced wind turbines are stall-inducted vibrations and blade flutter. Blades can undergo stall-induced oscillations once the wind turbine operates in the separation flow. The stall behaviour of the aerofoil induces energy in the blade structure, which excites the blade to vibrate. If the blade does not possess sufficient aerodynamic and structural damping factors, the external aerodynamic loads add more energy to the bade vibration. Examples of stall-induced vibrations in wind turbines are discussed in [5-8]. In the case of flutter, the blade vibrates at a frequency close to the natural frequencies of the blade structure [9]. As a modern wind turbine has three blades, a potential phase angle of vibration between blades is 120° which means that all three blades vibrate out of phase to each other by 120°. The limit of blade flutter in large-scale wind turbines was studied in [10], which showed that the unsteady aerodynamics of the flow has an impact on a flutter limit in wind turbine blades. It was also discussed that the physical properties of the blades, for instance, the centre of mass and the stiffness influenced blade flutter [11]. Dezvareh [12] investigated the effects of turbulence on the dynamic behaviour of an offshore wind turbine. Two models of normal and severe wind turbulence were employed, and the findings revealed that the amplitude of fluctuations of the dynamic response is enhanced by raising the amount of turbulence.

Precise calculation of aeroelastic instabilities in wind turbines, including blade flutter, is one of the main challenges in the renewable energy industry. While full-scale experiments are not always practically feasible, many small-scale experimental studies were conducted in the past years to investigate the aerodynamics of horizontal-axis wind turbine (HAWT) blades. Different

Published online: June 04 2021

configurations in which two wind turbines are arranged in in-line configuration [13] and offset configuration [14] are also experimentally studied to analyse the effect of a wind turbine on another. While the aerodynamics of wind turbines are broadly investigated in these experiments, the aeroelasticity or aeroelastic instabilities of wind turbines integrating the blade vibration are very difficult or sometimes impractical to be analysed experimentally and therefore, the majority of wind tunnel experiments focus on the aerodynamics of wind turbines. Besides, in most experiments, the different sources of flow instability and unsteadiness linked to the main physical parameters were ignored resulting in uncertainties. Hence, numerical methods and models have been developed to analyse both the aerodynamics and aeroelasticity of wind turbines, in which realistic environmental and physical conditions can be explored.

Computational Fluid Dynamics (CFD) models are efficient tools for the aerodynamic analysis of most engineering applications including wind turbines as they can provide accurate flow details depending on the turbulence modelling methods [15]. These models are used for the design and optimisation of wind turbines [16, 17]. For the aeroelasticity analysis, CFD models are often coupled with structural models to model and simulation the interaction between the fluid flow and the structure [18]. Coupling CFD models with Finite Element (FE) models are typically found in the aeroelasticity analysis of wind turbines as FE models provide flexibility in the structural modelling [19, 20]. Similarly, coupled CFD and Computational Structural Dynamics (CSD) are also used for the modelling of fluid-structure interactions and the aero-elastic analysis of wind turbines [21-23]. Besides, Multi-body Dynamics (MBD) models are also employed for the structural analysis and nonlinear motions of wind turbines as it considers the flexibility of wind turbine structures. [24], and they can also be coupled with fluid models. However, CFD models are computationally expensive. Significant computational resources and computation time are required for the unsteady simulations of fluid-structure interactions.

As the computation costs of highly accurate CFD methods remain the key challenge in the design of wind turbines. Frequency-domain methods such as harmonic balance methods were developed for fast and efficient computations for turbomachinery analysis [25, 26]. The harmonic solution technique of Rahmati et al. [27, 28] provides an alternative solution to the typical time-domain solution methods to model the harmonic flow disturbances and flow nonlinearities in turbomachines. Furthermore, Rahmati et al. [29, 30] proposed a nonlinear frequency-domain solution method to evaluate the aeroelastic performances of multi-stage turbines and multiple blade row configurations. Flow around an aerofoil of a turbine blade can be very complex and highly unsteady [31, 32]. The capability of a frequency-domain method was intensively investigated by Shine et al [33, 34] using direct numerical simulations, and they found that a frequency-domain method can resolve the highly unsteady and complex flow behaviours. Despite the fact that the frequency-domain methods are typically found in turbomachinery analysis, these methods are relatively new in the wind energy industry. Recently, a nonlinear harmonic method was applied to the aerodynamic and aeromechanical simulations of wind turbine rotors considering the inflow turbulence and wakes [35, 36]. Moreover, Shine et al. [37] proposed a nonlinear frequency-domain solution method for the aerodynamic and aeromechanical analysis of wind turbine rotors and complete wind turbine models, and it is found that this method is not only accurate but also computationally very efficient. A frequency-domain method was also applied to the aerodynamic simulations of multiple wind turbines due to its high capabilities [38]. Roy et al. [39] investigated the flow structure variations over a wind turbine blade with a high angle of attack. They used the SST k-w model to perform RANS simulations over the NACA4415 aerofoil. They found that the lift/drag ratio at the angles of attacks between 4° and6° was increased which is beneficial for the improved efficiency of small-scale wind turbines.

It is clear from the above literature review that the aeroelastic instabilities of wind turbine blades are very important and high-fidelity numerical methods are required for the accurate prediction of aeroelasticity parameters. The objective of this study is to use a highly efficient numerical method to examine the aerodynamic and aeromechanical performances, with detailed insight into the unsteady flow behaviour, of a WT blade aerofoil subject to the blade vibration at a wind range of operating conditions. The pressure variations over the surface of an aerofoil at various angles of attacks are also experimentally measured. Afterwards, a frequency-domain method is utilised for the aeromechanical simulations of a WT blade aerofoil to investigate the details of the flow field at a wide range of parameters, including angles of attack and Reynolds numbers. The results achieved from the frequency-domain solution are extensively compared to those of the time-domain solution to ensure accuracy.

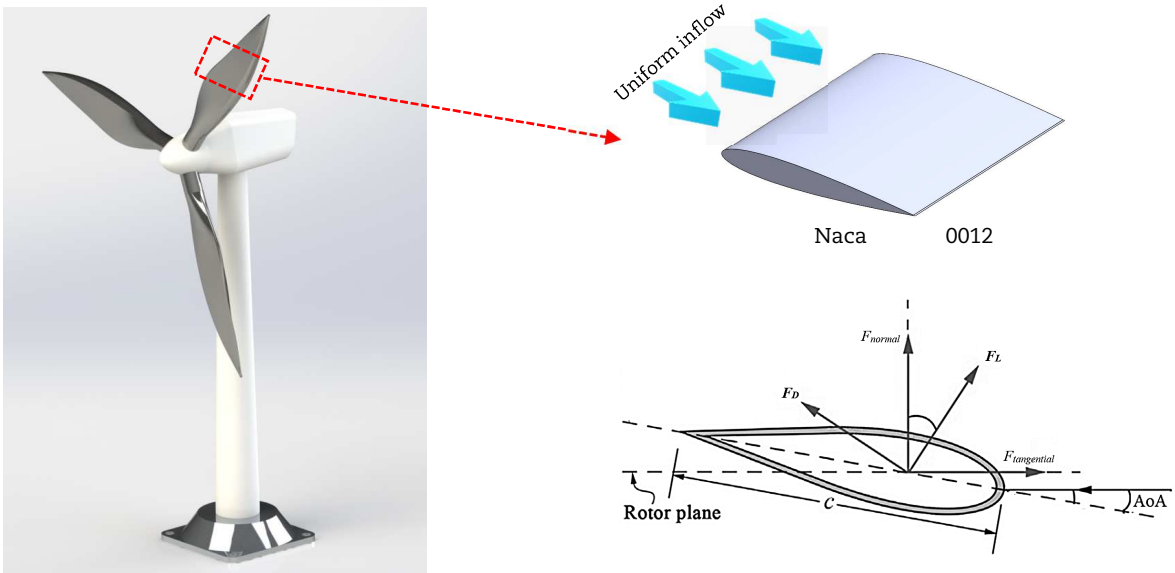

Fig. 1. Schematic diagram of the physical model of the NACA0012 aerofoil.

2. Experimental Setup

A wind turbine blade is typically composed of different types of aerofoils at different sections, and each section of the blade has a different pitch angle to optimise the lift coefficient. In this study, the NACA0012 is selected and assumed to be the mid-section of a wind turbine blade. Figure 1 shows the schematic diagram of the physical model of the mid-section of the wind turbine blade using the NACA0012 aerofoil. The chord length and the span of the physical model used in the experiment are 0.063 m and 0.049 m, respectively. The aerofoil has an effective surface area of 0.0031 m^2. The angle of attack of the aerofoil is varied between 0° to 25° during the experiment. The uniform freestream velocity (V_∞) is employed in the stream-wise directions, and the Reynolds number $\mathrm{Re} = V_\infty C / \nu$ is calculated based on the inflow speed and the chord length (C).

The selected NACA0012 aerofoil is placed inside a simple miniature wind tunnel of the AF10 airflow bench experiment. The AF10 airflow bench consists of a fan that collects the air from the environment and delivers it into the airbox, which sits above the wind tunnel. The airspeed flowing into the wind tunnel can be adjusted using a valve. The aerofoil is carefully fixed in the wind tunnel to ensure the air flows over the surfaces of the aerofoil and the flow is two-dimensional, representing the flow at the mid-section of a blade and avoiding tip vortices. The aerofoil and the wind tunnel are set up vertically. The aerofoil is rotatable to have the desired angle of attack (AoA). Pressure sensors are integrated on both pressure and suction surfaces of the aerofoil. The holes that appeared on the aerofoil surfaces indicate the locations of the pressure sensors. There are twelve pressure sensors over the aerofoil, including six sensors on each surface labelled by numbers. In addition to the aerofoil surfaces, three other pressure sensors are used to measure the pressure inside the airbox, the pressure at the inlet of the wind tunnel, and the atmospheric pressure. These pressure sensors are connected to the small pipes which come out of the wind tunnel and are then connected to the manometer to deliver the pressure data (see Figure 1 (a)).

The pressure measurements are indicated by the liquid inside the manometer. The liquid used is water, but it is coloured with a blue dye for clear visualisation. Before letting the airflow into the wind tunnel, the level of the liquid indicating the atmospheric datum is initially set so that the collected pressure measurements are relative to the atmospheric pressure. Although it is a small-scale wind tunnel experiment, the results and measurements can be scaled up for the analysis of larger aerofoils. In this experiment, the angles of attack are varied from 0° up to 20° with an increment of 5°, and the pressure distributions on the aerofoil surfaces are measured. The experiment is conducted at the Reynolds number of 4×10^6. The Reynolds number is calculated based on the inflow speed and the chord length. The details of the experimental setup are shown in Fig. 2.

3. Numerical Methodology

Figure 3 shows the computational domain and mesh generated for the simulations of the aerofoil. The domain is based on a two-dimensional model with a span-wise extension, known as a quasi-3D model, to analyse the two-dimensional flow at the blade mid-span. A hexahedral-type element is used throughout the domain. To capture the boundary layer separation and the flow around the aerofoil, the y^+ value is kept less than 1, and 20 layers of boundary layers are generated with a growth rate of 1.2. The inlet is located at a 3C distance from the leading edge, and the outflow is placed at 4C from the trailing edge, where C is the chord length. The far-field boundary is located at 2C from the aerofoil blade. After performing a grid independence study, the mesh size of 120×62×50 is employed for the CFD simulations.

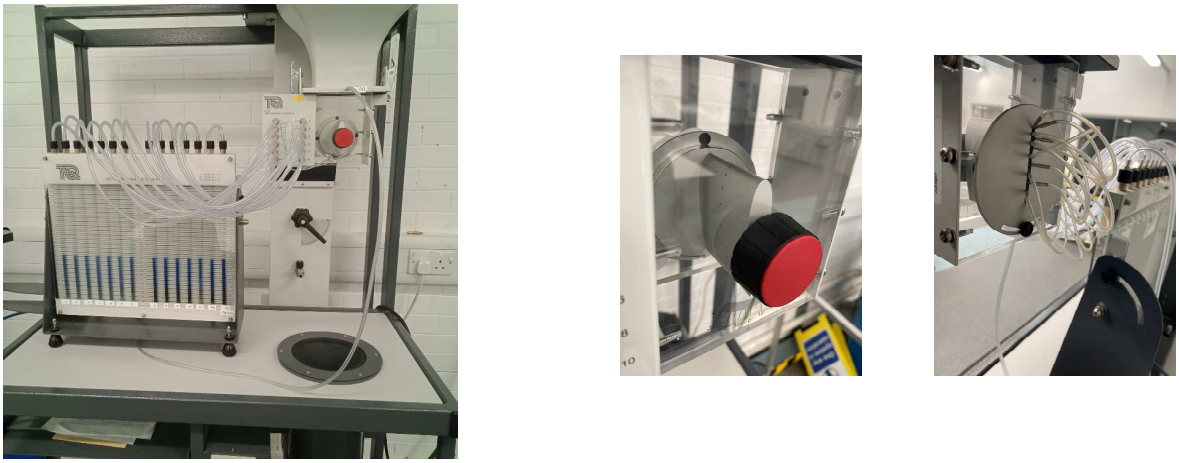

a) AF10 airflow bench and overall set-up

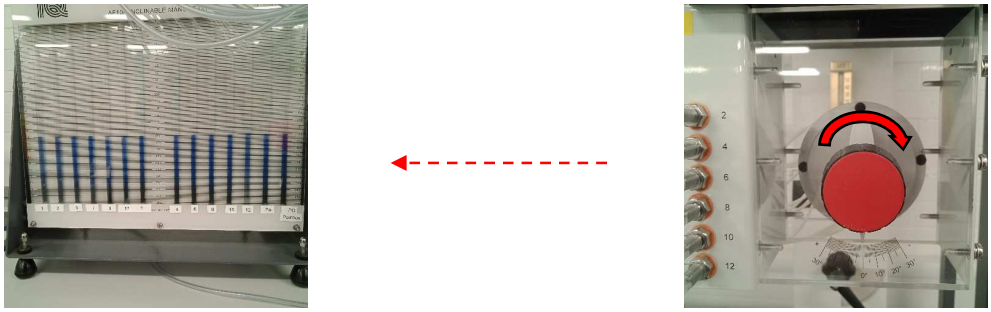

b) Aerofoil inside a wind tunnel and monometer

Fig. 2. Overall experimental set-up of the AF10 airflow bench experiment.

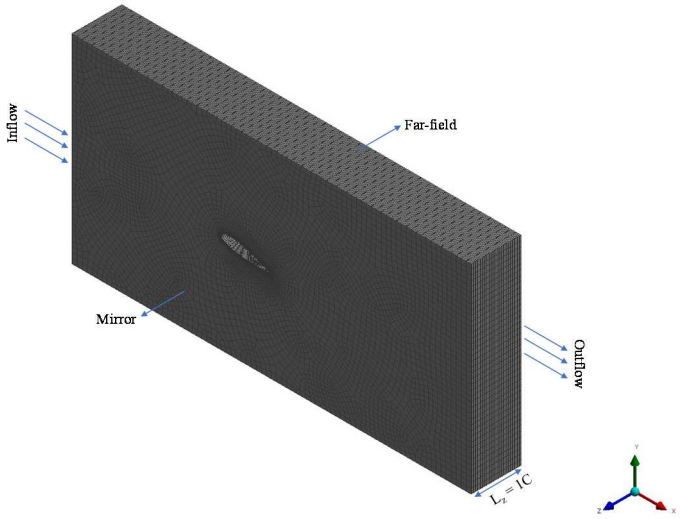

Computational domain with boundary conditions

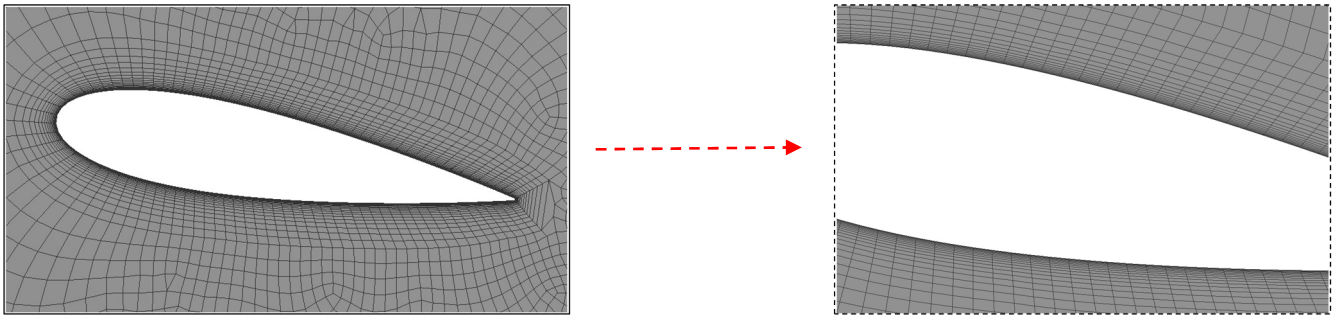

Blade-to-blade view of the mesh

Boundary layer mesh

Fig. 3. Details of computational domain and mesh with boundary conditions for the simulations of the wind turbine blade aerofoil.

The computations are performed by a 3D finite volume solver. The analysis was performed applying Unsteady Reynolds Averaged Navier-Stokes (URANS) model and the Navier-Stokes equations expressed in Cartesian coordinate can be written as [40]:

$$\frac{\partial}{\partial t}\int_{\Omega} Q d\Omega + \int_{S} \vec{F}_I . d\vec{S} + \int_{S} \vec{F}_V . d\vec{S} = \int_{\Omega} S_T d\Omega \tag{1}$$

in which Ω is the domain, S is the surface, Q is the vectors of the conventional parameters, S_T is the source term, and $\vec{F}_I$ and $\vec{F}_V$ are the inviscid and viscous terms, respectively. With employing the standard one-equation Spalart–Allmaras model, the above equation can be expressed as[40]:

$$\frac{\partial}{\partial t}(Q) = R(Q) \tag{2}$$

where R is the lumped residual. The inlet velocity is specified to have the required Reynolds number. A far-field boundary is specified in the pitch-wise direction and a symmetry boundary is defined on each surface of the domain in the span-wise direction. Stationary wall boundaries are used in the aerodynamic steady simulations, whereas deforming wall boundaries are employed in the aeromechanical simulations. The displacement of the wall deformation is defined as follow:

$$\delta(t) = \bar{\delta} + \delta_A \cos(\omega_i t) \tag{3}$$

where $\bar{\delta}$ and δ_A are the average and amplitude of the blade's movement. Consequently, the transient flow characteristics could be expressed by the Fourier series for a specified frequency, ⊠, and specific harmonic numbers (m), as shown in Eq. 4.

$$Q = \bar{Q} + \sum_{m=1}^{M}\left[A_Q \sin(m\omega t) + B_Q \cos(m\omega t)\right] \tag{4}$$

where $\bar{Q}$, A_Q and B_Q are the Fourier coefficients of the variable coefficients. Replacing the Fourier decomposition in the Navier-Stokes equation results in the following equations [37]:

$$\omega\sum_{m=1}^{M}\left[mA_Q \cos(m\omega t) - mB_Q \sin(m\omega t)\right] = R \tag{5}$$

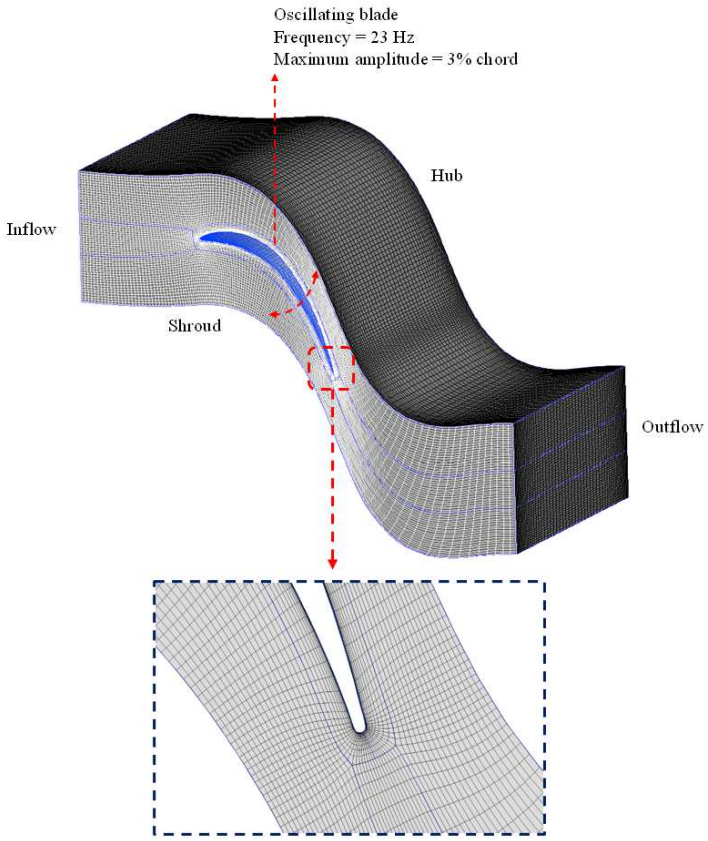

Fig. 4. Details of computational domain and mesh with boundary conditions generated for the simulations of the linear turbine cascade.

The resources of flow instability are based upon periodic blades movement, and therefore, Eqs. (4-5) can be expressed as:

$$Q = \bar{Q} + \left[A_Q \sin(m\omega t) + B_Q \cos(m\omega t)\right] \tag{6}$$

$$\omega\left[A_Q \cos(m\omega t) - B_Q \sin(m\omega t)\right] = R \tag{7}$$

4. Results and Discussion

4.1 Validation

In this paper, the IBPA of 180° case is reproduced using numerical simulations employing the frequency-domain method. The physical parameter including the vibration frequency and amplitudes are kept the same as the experiment. The Reynolds number of 2 $\times 10^5$ is used in both experiment and simulations. The computational domain and grid generated for the simulations are presented in Fig. 4. The mesh is generated using O4H topology in a structured grid generator. The generated mesh consists of 177 × 59 × 57 grid point distributions in the stream-wise, pitch-wise and span-wise directions, respectively. The blade, hub and shroud are treated as solid wall boundaries. A velocity inflow is applied at the inlet and a pressure outlet is defined at the outlet. The translational periodic boundary interfaces are applied in pitch-wise directions in order to represent a row of blades in a cascade.

The unsteady flow parameters due to the blade vibration can be separated into the time-averaged values and the unsteady perturbations. The transient pressure coefficient over the blade is mainly analysed in this study. The comparison of the average pressure coefficient (C_p) and the unsteady pressure coefficient (C_{p1}) variations on the surfaces of the aerofoil amongst the experiments and the numerical simulations using the proposed frequency-domain method for an IBPA of 180° is presented in Fig. 5. The results are extracted at different segments of the blade including 30%, 50% and 80% span sections. It is observed that the results are in excellent agreement, indicating that the frequency-domain method calculated the transient pressure distribution over the blade surfaces correctly. It is found that the unsteady perturbations are higher in the outer region of the blade where the vibration amplitude is larger. Apart from the unsteady pressure distribution, one of the most crucial aeroelasticity parameters in the design of turbomachinery is aerodynamic damping. The aerodynamic damping is computed by evaluating the aerodynamic work done per vibration period, and it is described as follow:

$$W = \int_{t_0}^{t_0+T} \int_A p\hat{\vec{v}}.\hat{n}\, dA\, dt \tag{8}$$

where t_0 is the initial time-step, T is the time take to complete a vibration cycle, p is the pressure of the fluid, v is the velocity of the blade subject to the deformed displacement, A is the surface area of the blade, and $\hat{n}$ is the normal unit vector. The aerodynamic damping for the blade of this linear turbine cascade for an IBPA of 180° acquired from the experiment and the simulations are compared in Table 1. It is seen that the results are in good agreement with each other.

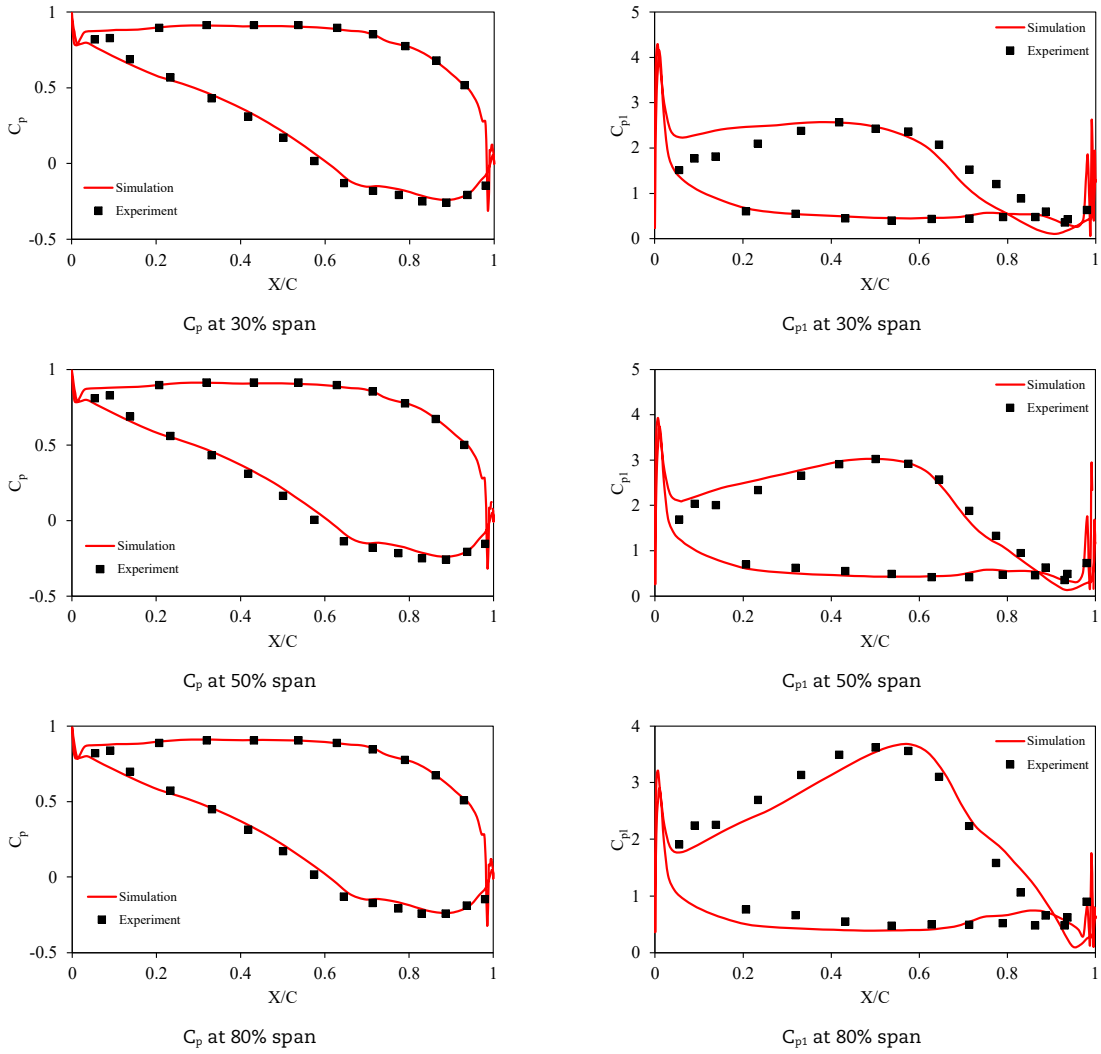

Fig. 5. Variations of pressure coefficient (C_p) and unsteady pressure amplitude coefficient (C_{p1}) at different sections of the blade of the linear turbine cascade.

4.2 Aerodynamic Analysis of Wind Turbine Aerofoil

Figure 6 demonstrates the pressure coefficients obtained from the experiment and the CFD simulations for different angle of attacks (AoAs). At AoA= 0°, the same amount of flow passes over both pressure and suction sides of the aerofoil due to its symmetric profile, which leads to the same pressure distributions on both surfaces of the aerofoil. Theoretically, there is no lift at this AoA. As the angle of attack is raised to 5°, the pressure difference between the two surfaces of the aerofoil starts to occur, generating a lift force. The pressure variation amongst the two sides becomes greater at AoA= 10° as the pressure on the pressure side becomes significantly larger than that of the suction surface, leading to an increased lift coefficient. At this angle, the flow starts to separate from the suction side closer to the trailing edge. When increasing the angle of attack further to 15°, a great deviation amongst the surfaces is seen in the region near the leading edge. The pressure difference is then reduced at around X/C=0.4 which continues up to the trailing edge. It is mainly because of the flow detachment from the suction side, and the flow separating point shifts in the direction of the leading edge as the AoA is increased. Due to the flow detachment, the recirculating flows and separated bubbles exist in the separation zone, which causes turbulence around the aerofoil. It can be noted that the flow behaviour is now similar to a stall nature at this AoA. At the angles of attack of 20° and 25°, it can be clearly seen that the pressure is not increased much near the leading edge compared to that of the 15°. However, the pressure difference between the two surfaces is significantly reduced afterwards, approximately from X/C=0.1. This indicates that the flow separation becomes too large, and the flow is separated nearly from the leading edge of the aerofoil, which results in a turbulent flow and flow recirculation on the suction surface and a loss of lift coefficient. Therefore, it can be concluded that the stall angle is past and the angles of attack of 20° and 25° fall within the post-stall region. Overall, raising the angle of attack leads to an inflow angle that causes a greater pressure difference between the two surfaces, which results in increased pressure and lift coefficients, before reaching its maximum at the stall angle. In terms of comparison between the experiment and the simulation for validation, it is seen that excellent agreement is obtained between the two methods.

Table 1. Aerodynamic damping

Method	Aerodynamic damping
Experiment	0.52
Simulation	0.57

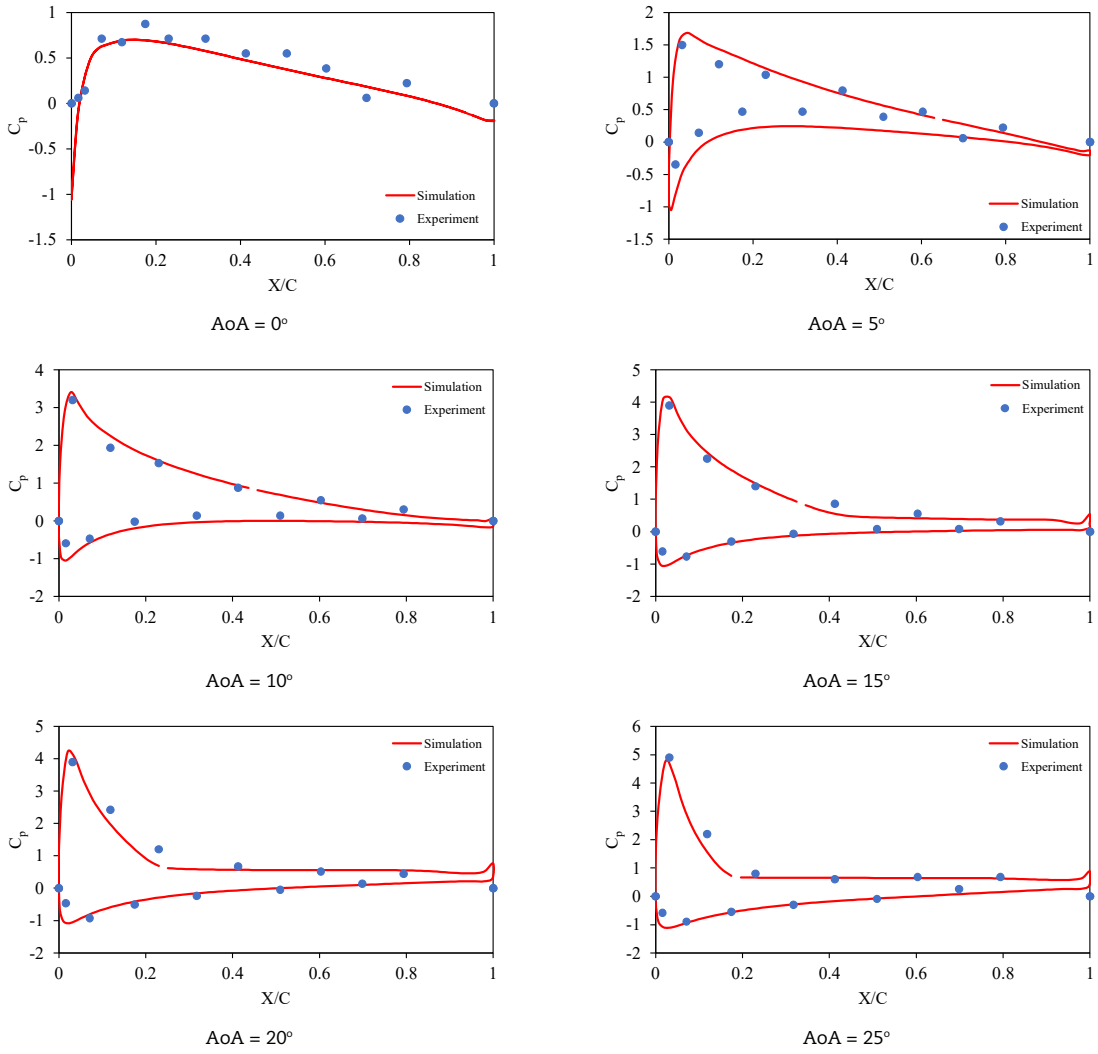

Fig. 6. Pressure coefficient at various angles of attack.

4.3 Aeromechanical Analysis of Wind Turbine Aerofoil at Various Angles of Attack

After having validated the numerical model against the experiment, the aeromechanical simulations of this aerofoil are performed by integrating the blade vibrations. The vibration frequency, adopted from the modal analysis of the MEXICO wind turbine model, is 15 Hz, and the oscillation amplitude is set to be 1%C. Because of the blade vibration, the flow is transient, and the flow variables change in time. As the blade is periodically oscillating, the unsteady flow parameters are also periodic in time. Among others, the unsteady pressure coefficient on the aerofoil surfaces is mainly analysed in the aeromechanical analysis as they are used for the calculation of the aeroelasticity parameters such as aerodynamic damping.

Due to the periodic oscillation, the unsteady pressure on the aerofoil surface could be divided into the time-averaged and the unsteady coefficients. Figure 7 presents the time-averaged pressure coefficient (C_p) and the unsteady pressure coefficient (C_{p1}) at different angles of attack. As the experiment is only available for the rigid aerofoil, the results from the frequency-domain solution using the blade vibration are verified based on the typical time-domain technique. As seen, C_p variations are very similar to those of the steady simulations as previously shown. This is expected because the blade oscillation is periodic, and therefore, C_p values are similar to those from the steady simulations. The maximum amplitudes of unsteady pressure coefficient are seen at the blade leading edge in all cases due to the interaction between the incoming flow and an oscillating aerofoil. However, at the angle of attack of 0°, the unsteady pressure distributions are almost the same on the pressure and suction surfaces due to the same amount of flow passing over the aerofoil. As the angle of attack is increased, the pressure fluctuations on the pressure and suction surfaces are different as the pressure surface usually possesses a higher pressure field due to an inflow angle. Furthermore, the harmonically oscillating aerofoil causes flow acceleration and deceleration over both surfaces of the aerofoil that imposes the sinusoidal pressure loads. The difference in unsteady pressure fluctuations is present up to X/C=0.3 and it becomes very small afterwards at both 5° and 10° angles of attack. It is observed that the results from the frequency-domain solution and the time-domain solution agree well with each other, indicating that the frequency-domain method computed the pressure deviations and distributions correctly.

Figure 8 illustrates the instantaneous pressure contours on the surfaces of the aerofoil at various angles of attack. At AoA=0°, the maximum pressure is seen near the leading from where the same amount of pressure is distributed over the pressure and suction surfaces, which results in zero lift. The contour indicates that the maximum pressure is found in the region closer to the leading edge where the inflow has interactions with the aerofoil. Then, the pressure is unevenly distributed over the aerofoil surfaces resulting in a higher pressure on the pressure surface whereas a lower pressure is observed on the suction surface. This pressure difference between the two surfaces starts to produce a lift force. At AoA=10°, the pressure difference between the two surfaces becomes larger, leading to a stronger lift. It is seen in the contour that the pressure on the suction surface is significantly lower than that of the pressure side.

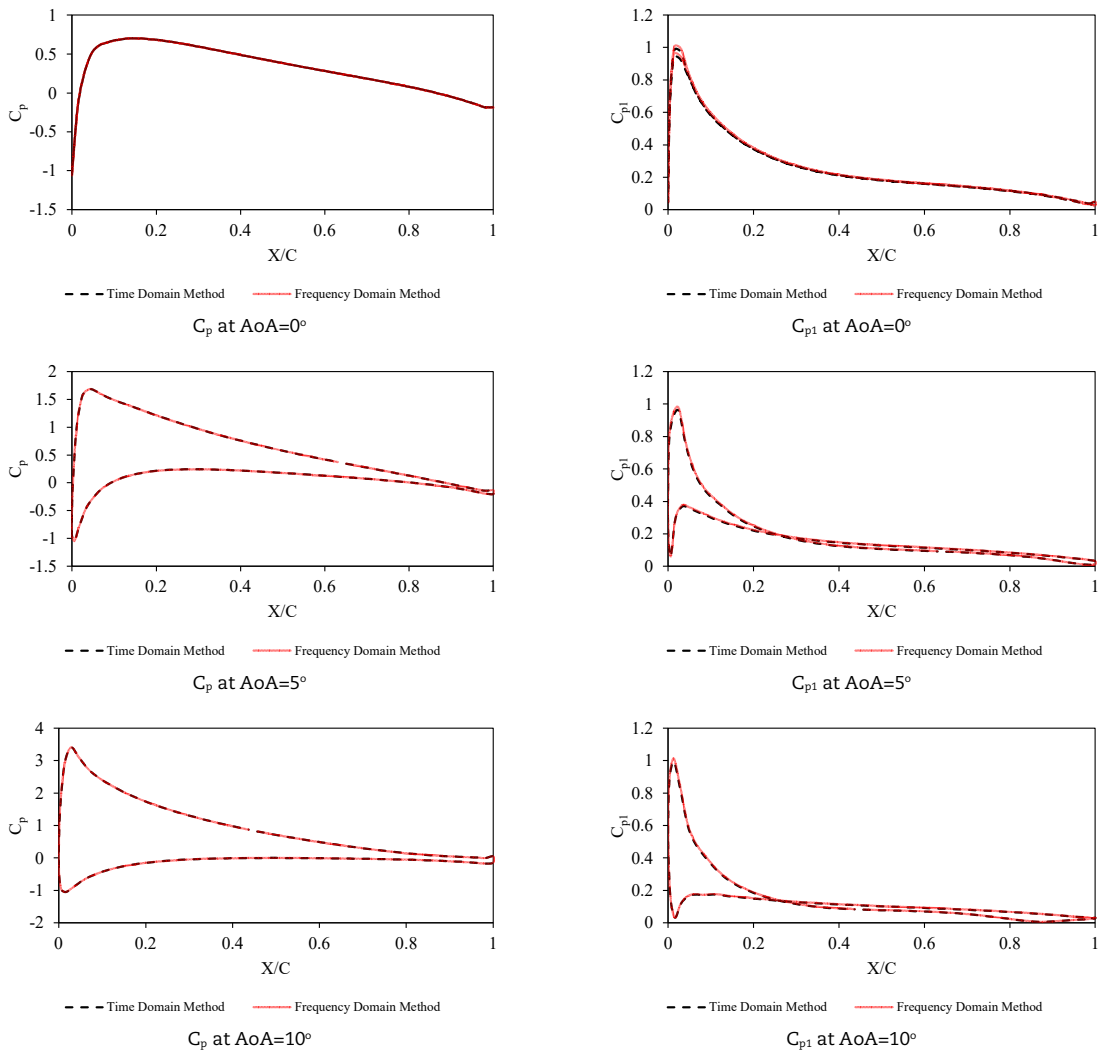

Fig. 7. Time-averaged pressure coefficient (C_p) and unsteady pressure amplitude coefficient (C_{p1}) at different angles of attack.

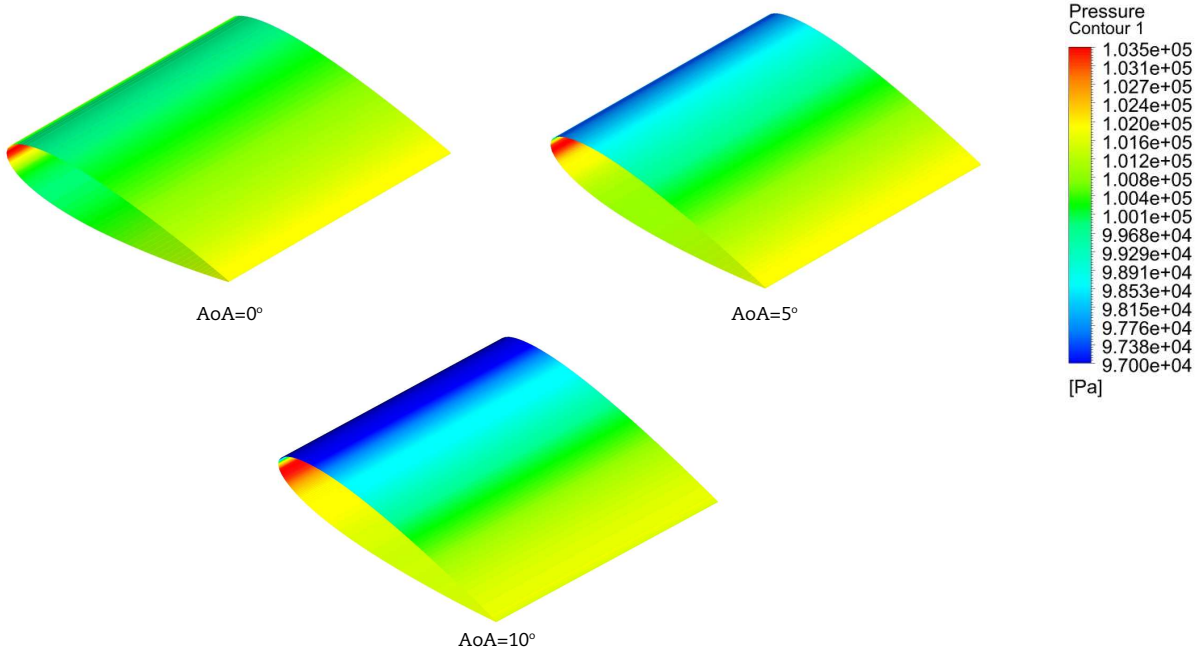

Fig. 8. Instantaneous pressure contours on the aerofoil surfaces at different angles of attack.

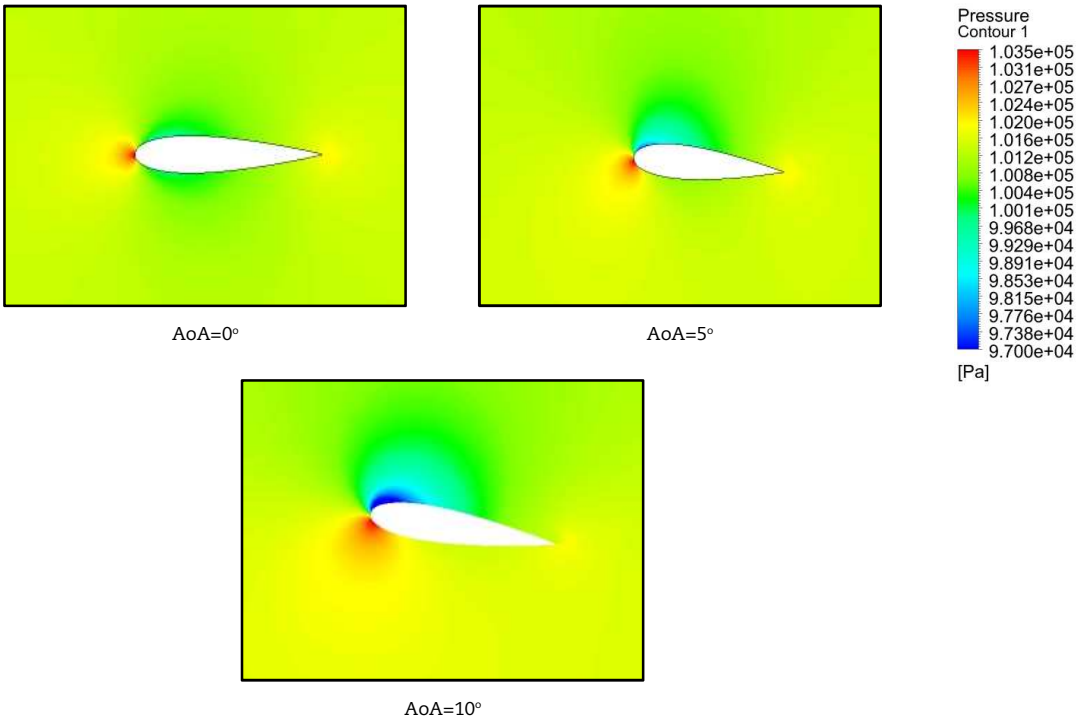

Fig. 9. Instantaneous pressure contours over the WT aerofoil at various AoAs.

Figure 9 shows the transient pressure contours near the aerofoil at various AoAs. When the angle of attack is 0°, as discussed, the pressure is maximum at the leading edge, and then, the pressure is distributed equally on the pressure and suction surfaces. Raising the angle of attack changes the stagnation point. At the angle of attack of 5°, the maximum pressure concentration is shifted marginally towards the pressure surface. As a result, the pressure on the suction surface is lower than that of the pressure surface. Increasing the angle of attack further to 10° makes the shift of the maximum pressure concentration towards the pressure surface even further and the pressure difference between the two surfaces even higher. It is seen that the pressure near the leading edge is much higher and stronger on the pressure surface compared to the suction surface, which leads to a greater variation in pressure distributions.

Theoretically, the pressure distribution around an aerofoil is inversely proportional to the velocity distribution. Figure 10 illustrates the instantaneous velocity contours around the aerofoil at various AoAs. The dimensionless velocity (V/V_{ref}) is provided for these contours. It is seen that the velocity is zero at the stagnation point where the flow interacts with the aerofoil whereas the pressure is maximum at this point. At the angle of attack of 0°, higher velocity fields are equally distributed over the aerofoil surfaces; however, lower pressure fields are seen on these surfaces in terms of pressure. At this AoA, the flow is attached to the aerofoil surface without a lift. At AoA=5°, it is obvious that the flow stagnation point shifts slightly towards the pressure surface as previously seen in the pressure contours. The relative velocity is then distributed over the suction surface, which leads to higher velocity distribution over the suction side. The flow is mostly attached to the aerofoil, but a very small flow separation is observed at the trailing edge. Raising the AoA to 10° makes the shift of the stagnation point toward the pressure surface even further. As a result, the flow with the high-velocity field is distributed over the suction surface until the aft region of the blade, from where the flow is separated. The velocity on the suction surface at this AoA is higher than at any other angles. Generally, with an inflow angle, the velocity is higher on the suction surface and lower on the pressure surface, whereas the pressure is higher on the pressure side and lower on the suction side.

The key parameter in the aeromechanical study of turbomachinery including wind turbines is the aerodynamic damping value which monitors the steadiness of the blade. If the aerodynamic damping is negative, it is possible that the blade vibration could undergo the flutter behaviour. In this study, the aerodynamic damping of the blade aerofoil at various AoAs are calculated using both frequency-domain and time-domain approaches, based on Eq. (8), to validate the accuracy of the frequency-domain solution on predicting the aeroelasticity parameter. The aerodynamic damping values obtained from both methods for various angles of attack are listed in Table 2. It is observed that the blade vibration is stable at the considered three angles of attack, and the aerodynamic damping is slightly increased when increasing the AoA from 0° to 10°. A good agreement in predicting the aerodynamic damping is obtained among the frequency-domain and time-domain methods. Consequently, it was deduced that the frequency-domain method has the capability to be utilised for the aeroelasticity analysis of WT blade aerofoils.

Table 2. Aerodynamic damping at different angles of attack.

Solution Method	AoA=0°	AoA=5°	AoA=10°
Frequency-domain Method	0.39	0.40	0.41
Time-domain Method	0.40	0.42	0.43

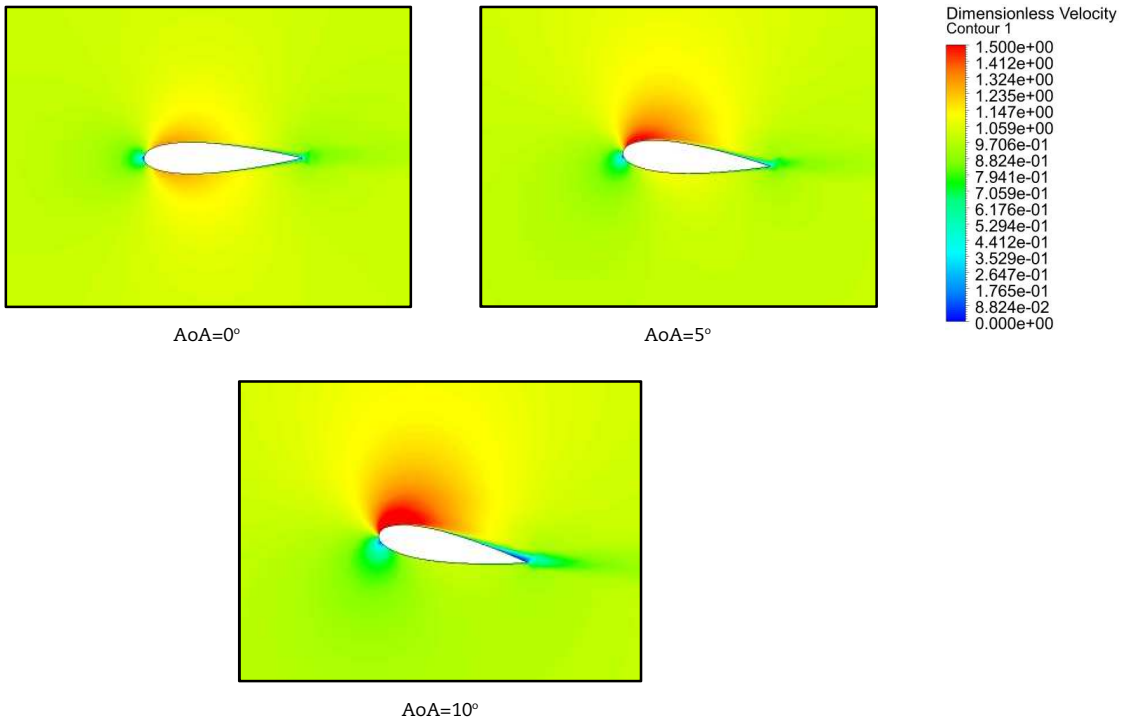

Fig. 10. Instantaneous dimensionless velocity (V/V_{ref}) contour around the aerofoil at different AoAs.

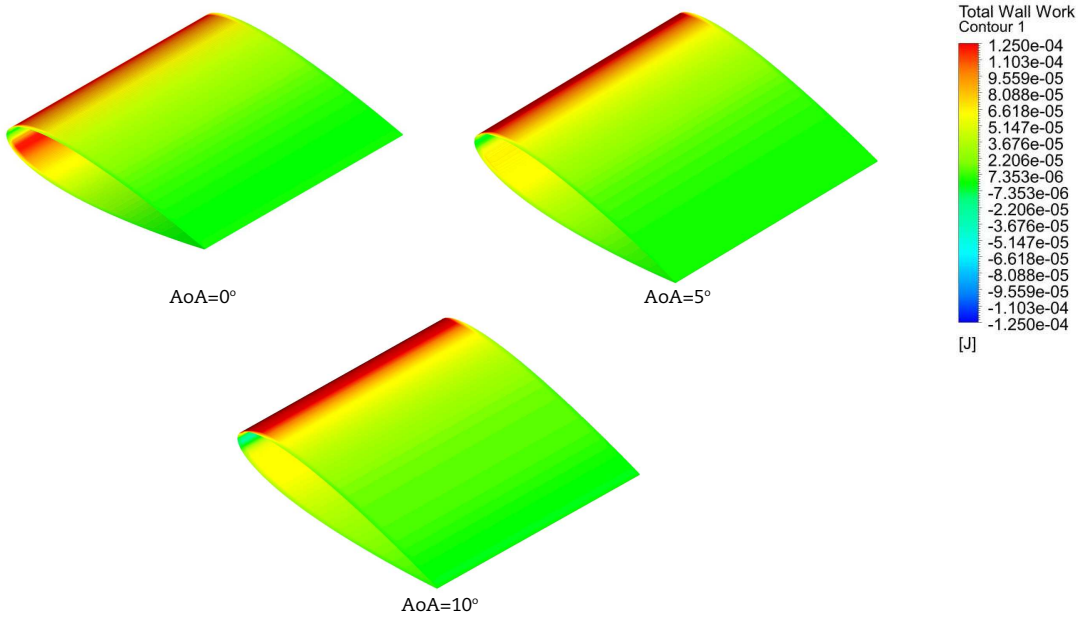

Fig. 11. Total wall work contour on the aerofoil surfaces at different angles of attack.

Figure 11 shows the total wall work distribution over the surfaces of the aerofoil, which is directly related to the calculation of the aerodynamic damping and the determination of the stability of the blade. The positive values of the total wall work contour represent the stabilising effect and the negative values correspond to the destabilising effect. It is seen that the aerofoil possesses a dominant stabilising effect at all angles of attack resulting in positive values of aerodynamic damping as previously discussed. The maximum stabilising effect is observed in the region around the leading edge. In details, at the angle of attack of 0°, these stabilising effects are equally present on both pressure and suction sides. By raising the AoA from 0° to 5° and 10°, it is found that the stabilising effect becomes stronger on the suction surface than on the pressure side.

4.4 Aeromechanical Analysis of Wind Turbine Aerofoil at Various Reynolds Numbers

Figure 12 depicts the variations of pressure coefficient (C_p) and (C_{p1}) at different Reynolds number. It is observed that the time-averaged pressure coefficient distribution is relatively the same at all Reynolds numbers. In terms of the unsteady pressure coefficient distribution, the maximum value is found at the leading edge where the flow interacts with the oscillating aerofoil. A great difference in unsteady pressure difference, however, is observed along the aerofoil at each Reynolds number. At Re = 4×10^5, The unsteady pressure amplitude coefficient gradually rises approximately from X/C=0.1 and reaches its second peak at around X/C=0.5, which then slowly drops. This indicates that the unsteady pressure fluctuation is high along the chord of the aerofoil at

lower Reynolds numbers. This is because the flow unsteadiness is intensified by an aerofoil oscillating at a lower Reynolds number that causes the flow detachment and vortex generation along the aerofoil. When the Reynolds number is increased to 8×10^5, a similar rising pattern of unsteady pressure and the behaviour of fluctuation is observed. Raising the Reynolds number further reduces this behaviour of unsteady pressure distribution along the chord. This is due to an increased inflow velocity that improves the overall resistance of the turbulent boundary layers. These observations indicate that the unsteady pressure fluctuation is more significant at lower Reynold numbers, and this effect can be diminished by raising the Reynolds number.

Figure 13 presents the instantaneous pressure contours for different Reynolds numbers. The contours are plotted using dimensionless pressure. It is observed that the pressure deviation amongst the pressure and suction sides is bigger at $Re = 4 \times 10^5$ than in any other cases. Compared to other Reynolds numbers, the pressure on the pressure surface is also much higher at $Re=4 \times 10^5$. Raising the Reynolds number reduces the pressure distinction between the two aerofoil sides. At $Re = 2 \times 10^6$ and $Re = 4 \times 10^6$, the pressure distribution is similar in both cases; the pressure difference is found to be greater at lower Reynolds numbers.

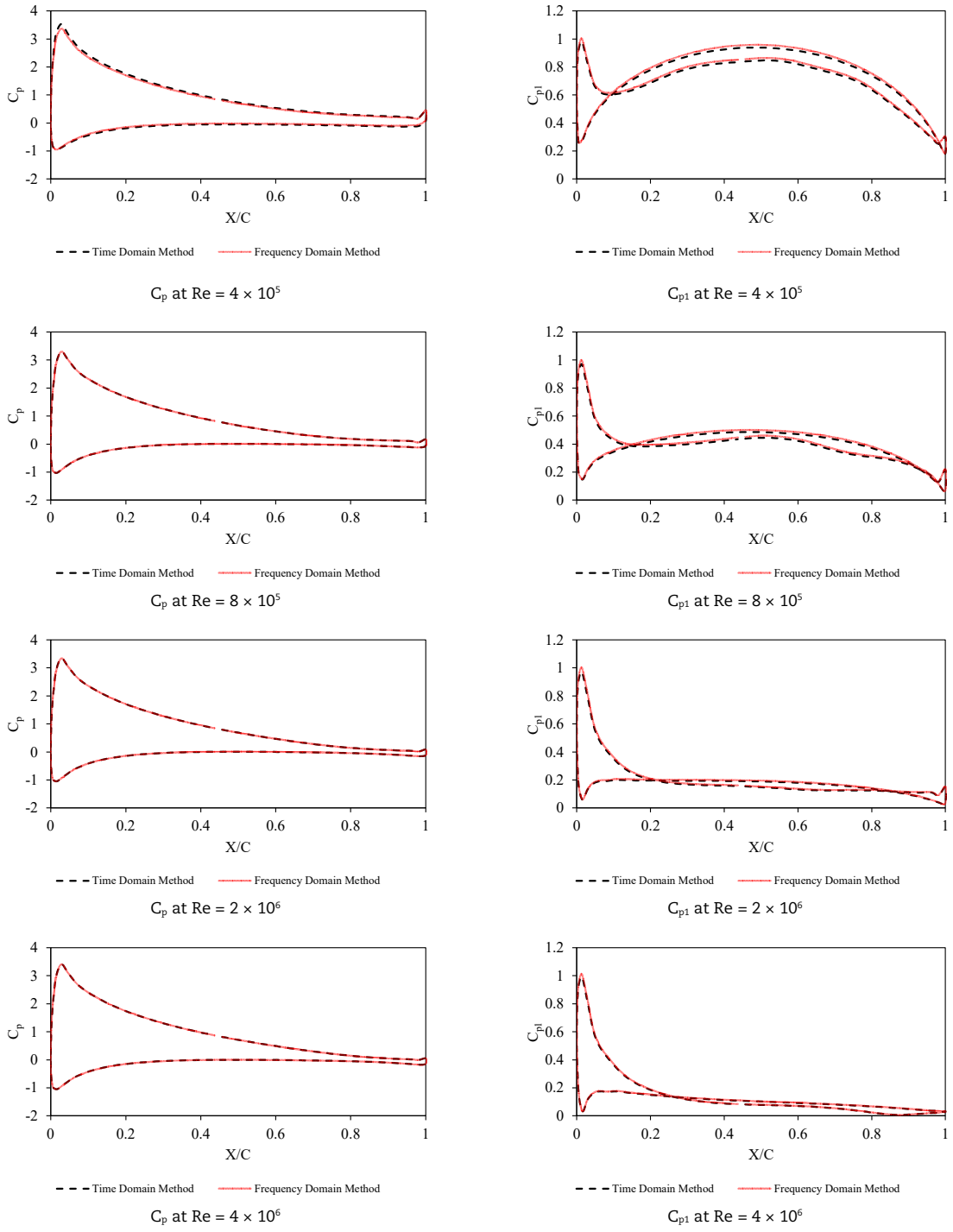

Fig. 12. Time-averaged pressure coefficient (C_p) and unsteady pressure amplitude coefficient (C_{p1}) at different Reynolds numbers.

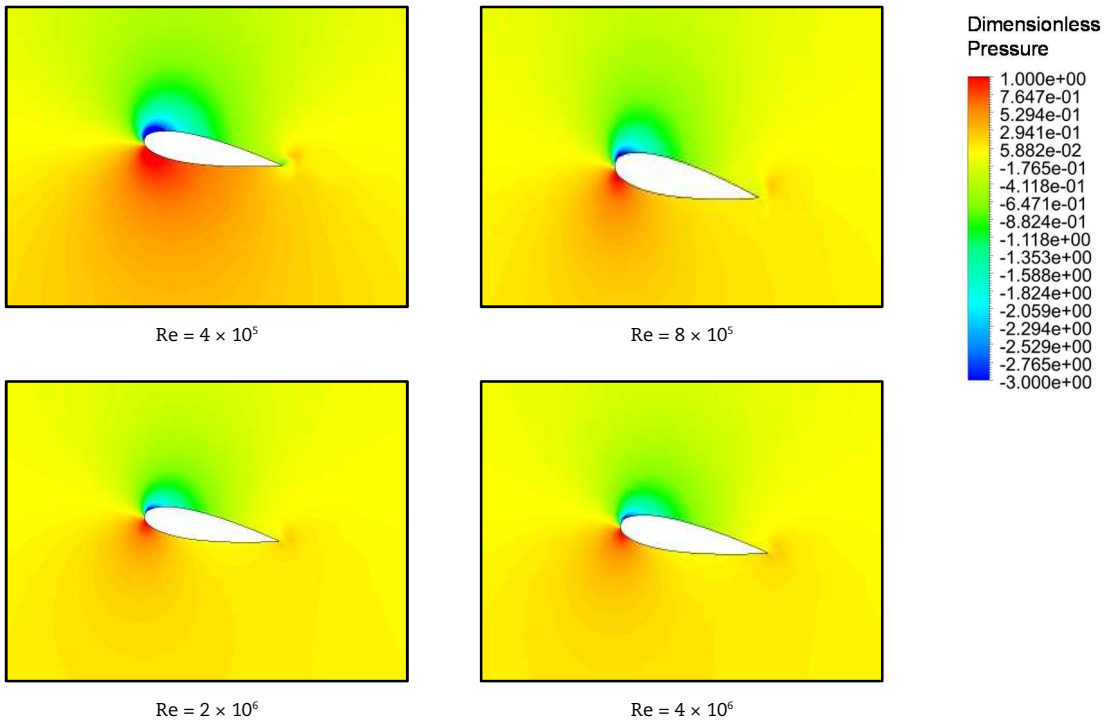

Fig. 13. Instantaneous dimensionless pressure contours at different Reynolds numbers.

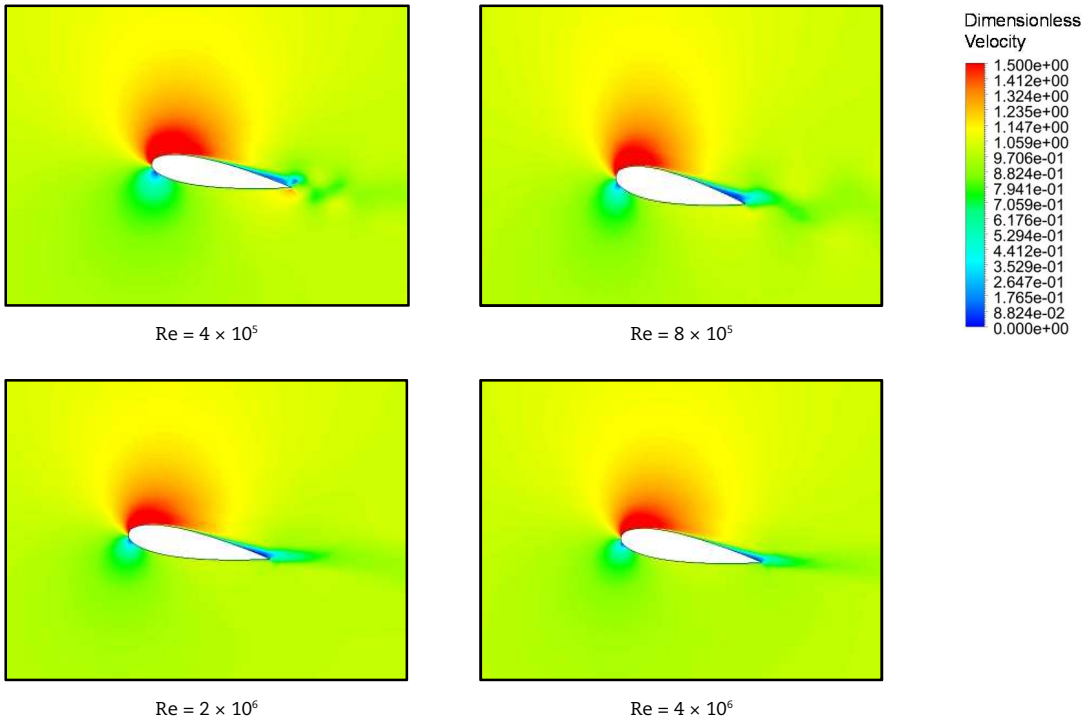

Fig. 14. Instantaneous dimensionless velocity contour at different Reynolds numbers.

The impact of Reynolds number on the flow field around the aerofoil can be visualised in terms of velocity distributions. The instantaneous dimensionless velocity contours around the aerofoil at different Reynolds numbers are demonstrated in Fig. 14. These velocity distributions are discussed based on an oscillating blade aerofoil. It is observed that the flow unsteadiness is higher at lower Reynolds numbers, whereas the flow separation is reduced at higher Reynolds numbers. The vortex structures left from the trailing edge are comparable to the Kárman vortex at Re = 4×10^5. Formation of the laminar vortex shedding and the laminar to turbulence transition are seen around the trailing edge; however, the vortex frequency is less significant at Re = 8×10^5. Vortex shedding behaviour is completely undetected at Re = 4×10^6 when the flow develops much stronger at higher Re numbers, which ultimately reduces the detached shear layers and recirculation. The turbulent boundary layer is more consistent at high Reynolds numbers.

Table 3. Aerodynamic damping at different Reynolds numbers.

Method	Re=4×10^5	Re=8×10^5	Re=2×10^6	Re=4×10^6
Frequency-domain Solution Method	0.05	0.08	0.18	0.41
Time-domain Solution Method	0.07	0.10	0.20	0.43

Similar to the previous analyses for different AoAs, the aerodynamic damping values are also calculated to examine the impact of different Reynolds number on the aeroelastic performance of the aerofoil. Likewise, the aerodynamic damping values are calculated using both frequency-domain and time-domain methods. It is found that the results achieved from the frequency-domain solution are in close agreement with the conventional time-domain solution (See Table 3). In terms of the effect of Reynolds number, it is seen that, although the aerodynamic damping values are positive at all Reynolds numbers, the aerodynamic damping is relatively low at Re=4 × 10^5 and 8 × 10^5, which gradually increases when raising the Reynolds number to 2 × 10^6. At Re = 4 × 10^6, the aerodynamic damping is larger than that of Re = 2 × 10^6 by 56% and that of Re = 4 × 10^5 by 88%. As discussed, the flow unsteadiness is higher due to vortex generation at lower Reynolds numbers. The vortex generation and pressure fluctuation, as previously seen, enforce aerodynamic forces on the blade. As the blade gains energy from the flow, it is possible that the blade vibration could lead to flutter instability when the aerodynamic damping is not sufficient enough to damp the vibration. Therefore, the selection of operating conditions, including Reynolds numbers, is very important for the design process of offshore wind turbine blades.

5. Conclusion

The aerodynamic and aeromechanical simulations of a WT blade aerofoil at different AoAs and various Reynolds numbers are presented in this paper. To confirm the precision of the numerical model, the simulation results are first compared to the experiment. It is found that the numerical results and the experimental results are in close agreement. The main conclusions are as follows:

- A nonlinear frequency-domain method, validated against the experiment conducted for a linear turbine cascade, is applied to the aeromechanical simulations of the wind turbine blade aerofoil. It is seen from the analysis at different AoAs that the difference in unsteady pressure distributions between the aerofoil surfaces increases as the angle of attack is raised.
- The flow is equally distributed over the surfaces of the aerofoil, and a small flow separation is detected on the suction surface of the aerofoil near the trailing edge when the angle of attack is raised to 10°. The aerodynamic damping is also calculated to investigate the blade stability at different angles of attack, it is noticed that the blade vibration is considered stable at all angles of attack as the aerodynamic damping values are positive. A dominant stabilising effect is detected at all angles, especially near the leading edge.
- Instantaneous pressure contours reveal that the pressure on the pressure surface of the aerofoil at Re = 4 × 10^5 is higher than in any other cases. Flow visualisations using instantaneous velocity contours show that the laminar vortex shedding is identified at lower Reynolds numbers. The flow separation and recirculation in the separation zone is also detected on the suction surface at these Reynolds numbers. This behaviour is reduced when raising Reynolds number as the flow is mostly attached to the surface with a small separation near the trailing edge.
- It is concluded that the flow separation is reduced by increasing the Reynolds number. The prediction of aerodynamic damping at various Reynolds numbers indicates that the aerodynamic damping is relatively low at lower Re numbers due to higher flow unsteadiness, which can potentially affect the blade stability. The aerodynamic damping is increased as the Reynolds number is raised, and it is the highest at Re = 4 × 10^6.
- Extensive validations between the frequency-domain solution method and the time-domain solution method show that the results obtained from both methods are in excellent agreement, ensuring that the frequency-domain solution is accurate. However, the frequency-domain method solves significantly quicker than the conventional time-domain method, and the computational cost is found to be decreased by 90%.

Author Contributions

S. Win Naung performed experiments and numerical simulations and wrote the manuscript; M. Erfanian Nakhchi modified the manuscript, improved the quality and structure of the manuscript; M. Rahmati supervised the project and proofread the manuscript.

Acknowledgements

The authors would like to acknowledge the financial support received from the Engineering Physics and Science Research Council of the UK (EPSRC EP/R010633/1).

Conflict of Interest

The authors declared no potential conflicts of interest with respect to the research, authorship, and publication of this article.

References

[1] Hau, E., Vibration Characteristics, Wind Turbines: Fundamentals, Technologies, Application, Economics, pp. 233-268, Berlin, Heidelberg: Springer Berlin Heidelberg, 2013.
[2] Rezaei, M. M., Behzad, M., Haddadpour, H., and Moradi, H., Aeroelastic analysis of a rotating wind turbine blade using a geometrically exact formulation, *Nonlinear Dynamics*, 89(4), 2017, 2367-2392.
[3] Chaviaropoulos, P. K., Politis, E. S., Lekou, D. J., Sørensen, N. N., Hansen, M. H., Bulder, B. H., Winkelaar, D., Lindenburg, C., Saravanos, D. A., Philippidis, T. P., Galiotis, C., Hansen, M. O. L., and Kossivas, T., Enhancing the damping of wind turbine rotor blades, the DAMPBLADE project, *Wind Energy*, 9(1-2), 2006, 163-177.
[4] Ramdenee, D., Ilinca, A., and Minea, I. S., Aeroelasticity of Wind Turbines Blades Using Numerical Simulation, *Advances in Wind Power*, 2012, 87-120.
[5] Hansen, M. H., Improved Modal Dynamics of Wind Turbines to Avoid Stall-induced Vibrations, *Wind Energy*, 6(2), 2003, 179-195.
[6] Hansen, M. H., Aeroelastic stability analysis of wind turbines using an eigenvalue approach, *Wind Energy*, 7(2), 2004, 133-143.
[7] Hansen, M. H., *Aeroelastic eigenvalue analysis of three-bladed wind turbines*, 2003, http://hdl.handle.net/20.500.11881/375.
[8] Thomsen, K., Petersen, J. T., Nim, E., Øye, S., and Petersen, B., A Method for Determination of Damping for Edgewise Blade Vibrations, *Wind Energy*,

3(4), 2000, 233-246.
[9] Patil, S., Zori, L., Galpin, P., Morales, J., and Godin, P., Investigation of Time/Frequency Domain CFD Methods to Predict Turbomachinery Blade Aerodynamic Damping.
[10] Lobitz, D. W., Aeroelastic stability predictions for a MW-sized blade, *Wind Energy*, 7(3), 2004, 211-224.
[11] Lobitz, D. W., Parameter Sensitivities Affecting the Flutter Speed of a MW-Sized Blade, *Journal of Solar Energy Engineering*, 127(4), 2005, 538-543.
[12] Dezvareh, R., Evaluation of turbulence on the dynamics of monopile offshore wind turbine under the wave and wind excitations, *Journal of Applied and Computational Mechanics*, 5(4), 2019, 704-716.
[13] Pierella, F., Krogstad, P.-Å., and Sætran, L., Blind Test 2 calculations for two in-line model wind turbines where the downstream turbine operates at various rotational speeds, *Renewable Energy*, 70, 2014, 62-77.
[14] Krogstad, P.-Å., Sætran, L., and Adaramola, M. S., "Blind Test 3" calculations of the performance and wake development behind two in-line and offset model wind turbines, *Journal of Fluids and Structures*, 52, 2015, 65-80.
[15] Wang, L., Liu, X., and Kolios, A., State of the art in the aeroelasticity of wind turbine blades: Aeroelastic modelling, *Renewable and Sustainable Energy Reviews*, 64, 2016, 195-210.
[16] Kaya, M. N., Kose, F., Ingham, D., Ma, L., and Pourkashanian, M., Aerodynamic performance of a horizontal axis wind turbine with forward and backward swept blades, *Journal of Wind Engineering and Industrial Aerodynamics*, 176, 2018, 166-173.
[17] Lee, H. M., and Kwon, O. J., Performance improvement of horizontal axis wind turbines by aerodynamic shape optimization including aeroealstic deformation, *Renewable Energy*, 147, 2020, 2128-2140.
[18] Liu, Y., Xiao, Q., Incecik, A., Peyrard, C., and Wan, D., Establishing a fully coupled CFD analysis tool for floating offshore wind turbines, *Renewable Energy*, 112, 2017, 280-301.
[19] Dai, L., Zhou, Q., Zhang, Y., Yao, S., Kang, S., and Wang, X., Analysis of wind turbine blades aeroelastic performance under yaw conditions, *Journal of Wind Engineering and Industrial Aerodynamics*, 171, 2017, 273-287.
[20] Wang, L., Quant, R., and Kolios, A., Fluid structure interaction modelling of horizontal-axis wind turbine blades based on CFD and FEA, *Journal of Wind Engineering and Industrial Aerodynamics*, 158, 2016, 11-25.
[21] Dose, B., Rahimi, H., Herráez, I., Stoevesandt, B., and Peinke, J., Fluid-structure coupled computations of the NREL 5 MW wind turbine by means of CFD, *Renewable Energy*, 129, 2018, 591-605.
[22] Dose, B., Rahimi, H., Stoevesandt, B., and Peinke, J., Fluid-structure coupled investigations of the NREL 5 MW wind turbine for two downwind configurations, *Renewable Energy*, 146, 2020, 1113-1123.
[23] Yu, D. O., and Kwon, O. J., Predicting wind turbine blade loads and aeroelastic response using a coupled CFD–CSD method, *Renewable Energy*, 70, 2014, 184-196.
[24] Wang, L., and Sweetman, B., Multibody dynamics of floating wind turbines with large-amplitude motion, *Applied Ocean Research*, 43, 2013, 1-10.
[25] Hall, K. C., Thomas, J. P., and Clark, W. S., Computation of Unsteady Nonlinear Flows in Cascades Using a Harmonic Balance Technique, *AIAA Journal*, 40(5), 2002, 879-886.
[26] He, L., Harmonic Solution of Unsteady Flow Around Blades with Separation, *AIAA Journal*, 46(6), 2008, 1299-1307.
[27] Rahmati, M. T., He, L., and Wells, R. G., Interface Treatment for Harmonic Solution in Multi-Row Aeromechanic Analysis, Turbo Expo: Power for Land, Sea, and Air, 2010, 1253-1261.
[28] Rahmati, M., He, L., and Li, Y., Multi-row interference effects on blade aeromechanics in compressor and turbine stages, Proceedings of the 13th International Symposium on Unsteady Aerodynamics, Aeroacoustics and Aeroelasticity of Turbomachines, 2012.
[29] Rahmati, M. T., He, L., and Li, Y. S., The Blade Profile Orientations Effects on the Aeromechanics of Multirow Turbomachines, *Journal of Engineering for Gas Turbines and Power*, 138(6), 2015, 062606.
[30] Rahmati, M. T., He, L., Wang, D. X., Li, Y. S., Wells, R. G., and Krishnababu, S. K., Nonlinear Time and Frequency Domain Methods for Multirow Aeromechanical Analysis, *Journal of Turbomachinery*, 136(4), 2013, 041010.
[31] Nakhchi, M. E., Naung, S. W., and Rahmati, M., High-resolution direct numerical simulations of flow structure and aerodynamic performance of wind turbine airfoil at wide range of Reynolds numbers, *Energy*, 225, 2021, 120261.
[32] Nakhchi, M. E., Win Naung, S., and Rahmati, M., DNS of secondary flows over oscillating low-pressure turbine using spectral/hp element method, *International Journal of Heat and Fluid Flow*, 86, 2020, 108684.
[33] Naung, S. W., Rahmati, M., and Farokhi, H., Numerical Investigation of the Effect of Flutter Instability of the Blade on the Unsteady Flow in a Modern Low-Pressure Turbine.
[34] Win Naung, S., Rahmati, M., and Farokhi, H., Direct Numerical Simulation of Interaction between Transient Flow and Blade Structure in a Modern Low-Pressure Turbine, *International Journal of Mechanical Sciences*, 192, 2021, 106104.
[35] Win Naung, S., Rahmati, M., and Farokhi, H., Aeromechanical Analysis of Wind Turbines Using Non-Linear Harmonic Method.
[36] Win Naung, S., Rahmati, M., and Farokhi, H., Aerodynamic Analysis of a Wind Turbine With Elevated Inflow Turbulence and Wake Using Harmonic Method.
[37] Naung, S. W., Rahmati, M., and Farokhi, H., Nonlinear frequency domain solution method for aerodynamic and aeromechanical analysis of wind turbines, *Renewable Energy*, 167, 2021, 66-81.
[38] Wacks, D. H., Nakhchi, M. E., and Rahmati, M., Forced Response of a Low-Pressure Turbine Blade using Spectral/hp Element Method: Direct Numerical Simulation, *Journal of Applied and Computational Mechanics*, 7(1), 2021, 135-147.
[39] Roy, A., Mallik, A. K., and Sarma, T. P., A Study of Model Separation Flow Behavior at High Angles of Attack Aerodynamics, *Journal of Applied and Computational Mechanics*, 4(4), 2018, 318-330.
[40] Naung, S. W., Nakhchi, M. E., and Rahmati, M., High-fidelity CFD simulations of two wind turbines in arrays using nonlinear frequency domain solution method, *Renewable Energy*, 174, 2021, 984-1005.

ORCID iD

Shine Win Naung https://orcid.org/0000-0001-8441-0725
Mahdi Erfanian Nakhchi https://orcid.org/0000-0003-1034-6091
Mohammad Rahmati https://orcid.org/0000-0003-4903-5370

How to cite this article: Naung S.W., Author M.E., Rahmati M. An Experimental and Numerical Study on the Aerodynamic Performance of Vibrating Wind Turbine Blade with Frequency-Domain Method, *J. Appl. Comput. Mech.*, 7(3), 2021, 1737–1750. https://doi.org/10.22055/JACM.2021.37406.3011